

Assessment of VIIRS Day-Night Band High Gain Calibration Using Stars

Xiaoxiong Xiong¹, Truman Wilson², and Kevin Vermeesch³

¹*Sciences and Exploration Directorate, NASA GSFC, Greenbelt, MD 20771, USA*

²*Science Systems and Applications, Inc., 10210 Greenbelt Road, Lanham, MD 20706, USA*

³*Global Science & Technology, Inc., 7501 Greenway Center Drive, Greenbelt, MD 20770, USA*

ABSTRACT

The VIIRS day-night band (DNB) operates in three different gain stages: low, mid, and high gain stage (LGS, MGS, and HGS), which enable an extremely large dynamic range with the HGS being sensitive to various low-light scenes. Similar to the reflective solar bands (RSB), the DNB uses an on-board solar diffuser for its LGS calibration, whereas the DNB MGS and HGS are calibrated using a relative approach that is tied to its LGS calibration. In this paper, we provide an assessment of VIIRS DNB HGS calibration stability or on-orbit gain trending using stars that appear in the field-of-view of its space view port. In addition to strategies and procedures adopted to process and analyze the gain trending, we discuss some of the challenges and limits of this approach, including the use of the modulated relative spectral response of S-NPP VIIRS resulting from wavelength-dependent mirror degradation. With the same stars, this approach can support inter-comparison of DNB HGS calibrations among different VIIRS instruments. Our results show that the star-based response trending for the VIIRS DNB HGS is generally consistent with that derived from its on-board solar diffuser. The calibration difference between S-NPP and N20 VIIRS DNB HGS is about 2%. This, together with their calibration differences at LGS and MGS, requires additional effort and mitigation strategy in support of high quality research activities and applications that combine input data from both sensors.

Keywords: VIIRS, DNB, calibration, inter-comparison, stars

1. INTRODUCTION

The Visible Infrared Imaging Radiometer Suite (VIIRS) instrument is currently operated on-board the Suomi NPP (S-NPP) and NOAA 20 (N20) satellites, launched in October 2011 and November 2017, respectively. Nearly identical VIIRS instruments will also fly on-board future JPSS satellites, JPSS-2, -3, and -4 that are planned for launch in 2022, 2028, and 2032, respectively [1-3]. The VIIRS makes visible and long-wave infrared observations of the Earth's land, atmosphere, cryosphere and oceans with a global coverage twice a day and generates many critical environmental products that are used extensively to monitor and study the land, sea, and ice surface temperatures, fires, vegetation index, snow and ice cover, ocean color properties, clouds and aerosols. Many of the VIIRS data products further extend and improve upon those developed from observations made by its heritage sensors, such as AVHRR and MODIS [3-7].

The VIIRS uses a rotating telescope assembly (RTA) and collects data in 22 spectral bands with wavelengths from 0.4 to 12.2 μm , including 14 reflective solar bands (RSB), 7 thermal emissive bands (TEB), and a panchromatic band that has a broad spectral response from 0.5 to 0.9 μm . This panchromatic band can sense reflected light from space during both day and nighttime, thus referred to as the day-night band (DNB). It operates in three different gain stages: low, mid, and high gain stage (LGS, MGS, and HGS), thus covering a very large dynamic range. Its HGS is extremely sensitive and able to respond to various low-light scenes at nighttime. Table 1 provides a summary of key design requirements for the VIIRS DNB [8-9]. In addition to various environmental products mentioned above, the VIIRS sensor has enabled many unique applications based on its DNB nighttime observations, including monitoring and studies of the patterns and trends of city lights, nighttime fires, fishing boats, and aurora borealis [10-11]. As expected, the quality of the data products and

applications derived using DNB observations depends strongly on its calibration accuracy, as well as the calibration consistency among different VIIRS instruments.

Table 1. Key design and calibration requirements for VIIRS DNB.

Spectral Bandwidth	0.5 - 0.9 μm
Lmin (HGS)	$3.0 \times 10^{-5} \text{ W/m}^2/\text{sr}$
Lmax (LGS)	$2.0 \times 10^2 \text{ W/m}^2/\text{sr}$
SNR at HGS Lmin and scan angle $< 53^\circ$	6
SNR at HGS Lmin and scan angle $\geq 53^\circ$	5
Uncertainty for LGS (Lmax - Lmin)	5-10%
Uncertainty for MGS (Lmax - Lmin)	10-30%
Uncertainty for HGS (Lmax - Lmin)	30-100%

The VIIRS DNB LGS calibration is performed using an on-board solar diffuser (SD) and solar diffuser stability monitor (SDSM) system and its MGS and HGS calibrations are derived using a relative approach via gain ratios of MGS to LGS and HGS to MGS. This paper provides an assessment of VIIRS DNB HGS calibration by using stars observed through its space view (SV) port. It describes various strategies and procedures implemented in this approach to monitor the DNB HG calibration stability or its on-orbit gain trending. Also discussed are some of the complications and limits to this approach. Since both S-NPP and N20 VIIRS are able to view the same stars at nearly the same time, this approach can support their DNB HGS calibration inter-comparisons. Results from this study show that the DNB HGS responses derived from star observations are in trend with those derived from on-board solar diffuser observations for both S-NPP and N20, with star responses trending slightly lower than SD responses. The DNB HGS calibration difference between S-NPP and N20 VIIRS is about 2% after corrections for sensor specific characteristics. Calibration differences between S-NPP and N20 also exist for DNB LGS and other RSB [12-14]. The root cause for the calibration difference between S-NPP and N20 VIIRS in the solar reflective region remains to be investigated and, as a result, special efforts or mitigation strategies are needed for various studies and applications that use data from both sensors.

2 DNB ON-ORBIT CALIBRATION

The VIIRS DNB is a temperature-controlled charge-coupled device with four detector arrays: one for the LGS, one for the MGS, and two for the redundant HGS (i.e., the HGA and HGB). Figure 1 is a schematic of the VIIRS DNB detector arrays, with each having 672 subpixel detectors in the track direction that are aggregated to form 16 along-track pixels. In the scan direction, the LGS, MGS, HGA, and HGB detector arrays have 1, 3, 250, and 250 sub-pixel detectors, respectively. Both MGS and HGS operate in a time delay integration (TDI) mode with their along-scan sub-pixel detectors. Designed to maintain near-constant spatial resolution, the DNB detectors collect data in 32 different aggregation modes on each side of nadir with varying sub-pixel detectors in both along scan and track directions and with different data sampling rates [15]. Hence, the VIIRS DNB calibration is gain, detector, aggregation mode, and half-angle mirror (HAM) side dependent.

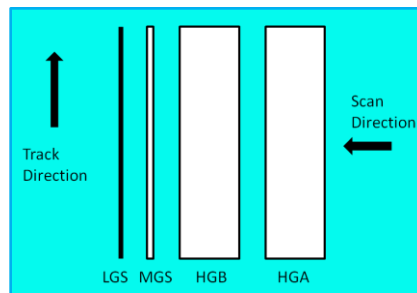


Figure 1. Schematic layout of VIIRS DNB detector arrays.

The DNB LGS is typically used to observe daytime scenes and its on-orbit calibration is traceable to the on-board SD, similar to the calibrations for other RSB. For a given detector, aggregation mode, and HAM side, the DNB LGS calibration coefficient (F_{LGS}) can be computed using the following expression,

$$F_{LGS} = L_{SD} / (dn_{SD} / RVS_{SD}) \quad (1)$$

where L_{SD} is the spectral band integrated radiance reflected off the SD at the time of each calibration, dn_{SD} is the corresponding detector response with background (or dark offset) subtracted, and RVS_{SD} is the response versus scan angle (RVS) at the SD angle of incidence (AOI) relative to the HAM. In general, it takes at least 2 (HAM sides) \times 32 (aggregation modes) = 64 scans to complete a DNB calibration cycle. However, including the 4 calibration aggregation modes, it takes 72 scans for the full calibration cycle. As a result, the DNB SD F-factors are generated on a daily basis using the averages over multiple orbits.

The DNB MGS and HGS calibration uses a relative approach via gain ratios that are traceable to the LGS,

$$F_{MGS} = F_{LGS} \cdot (dn_{LGS} / dn_{MGS}) \quad (2)$$

$$F_{HGS} = F_{MGS} \cdot (dn_{MGS} / dn_{HGS}) \quad (3)$$

The LGS to MGS response ratio is computed using a select region where the LGS is sensitive enough while the MGS response does not saturate. This gain ratio ties the MGS calibration coefficients to the LGS. The same process applies to transfer the calibration from MGS to HGS. The absolute calibration for the LGS requires fully illuminated SD responses (i.e. the scans with solar declination angles between 14° and 18°, also known as the sweet spot), whereas the MGS to LGS and HGS to MGS ratios are computed using regions that are partially illuminated (i.e., scans outside the sweet spot range). More details on the VIIRS DNB calibration methodologies are provided in a number of references [16-18]. It is worth mentioning that the N20 VIIRS DNB operates with 22 aggregation modes. This option was adapted to reduce the impact of detector nonlinear responses at large aggregation modes [19].

Illustrated in Figure 2 are two examples of the DNB HGS responses or gains (1/F factors) for S-NPP. In general, the responses at different aggregation modes and detectors show similar trends. This is a useful feature, which allows DNB HGS calibration stability to be monitored by combining the relative responses from different detectors and aggregation modes. The large decrease of S-NPP DNB responses, especially at its mission beginning, was due to degradation of the sensor optics. Figure 3 shows similar examples for N20 VIIRS. Clearly, its DNB responses have been very stable since launch.

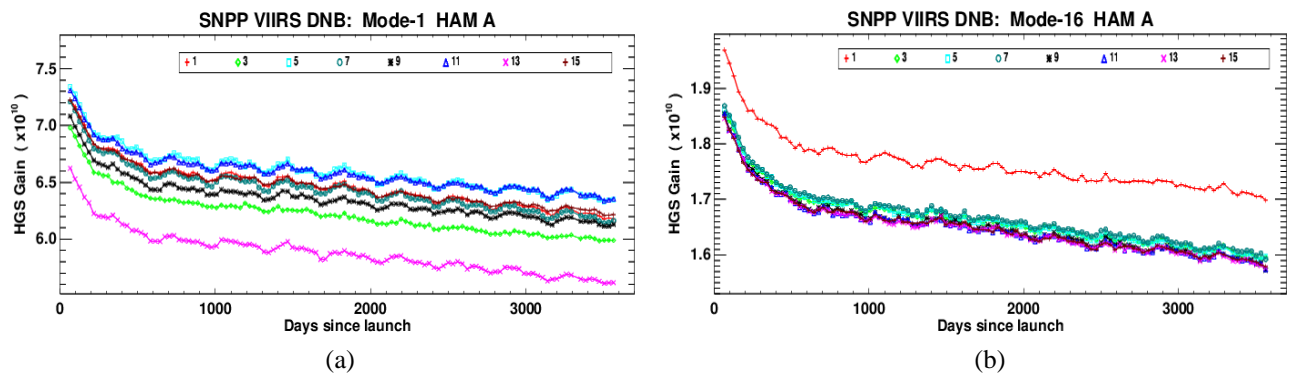


Figure 2. S-NPP VIIRS DNB HGS detector gains (1/F-factors): (a) aggregation mode-1 and (b) aggregation mode-16 (monthly averages, odd detectors, HAM A)

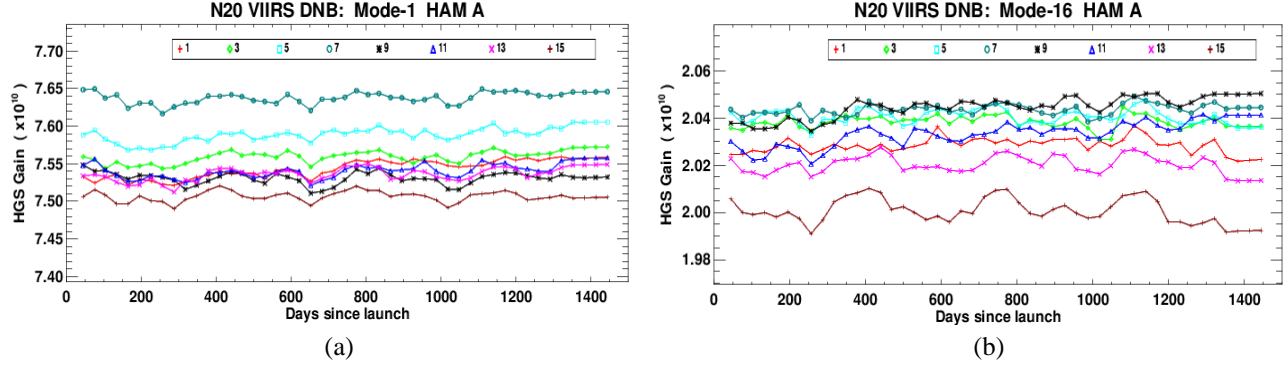


Figure 3. N20 VIIRS DNB HGS detector gains (1/F-factors): (a) aggregation mode-1 and (b) aggregation mode-16 (monthly averages, odd detectors, HAM A)

3 CALIBRATION STABILITY AND INTER-COMPARISON ASSESSMENT USING STARS

For VIIRS, star observations are made through its SV, which is an extension of the Earth-view (EV) port. For most stars, the spectral output is stable over the lifetime of satellite missions and therefore can be used as a source for instrument calibration. Although typical spectral irradiances of stars are much lower than that of the Moon, which is used for the DNB LGS calibration in addition to the SD, the DNB HGS is sensitive enough to observe to these stars over a wide range of signal levels [20]. In this work, we use observations for stars in the Yale Bright Star Catalog (BSC), which is a database of 9110 bright stars containing coordinates, spectral information, and other stellar characteristics [21].

The specific time that a star appears in the SV depends on its celestial coordinates (right ascension and declination), orientation of the satellite orbit, and the pointing direction of the SV. In celestial coordinates, both VIIRS instruments are able to observe stars in the declination range from -15 to 32 degrees over all right ascension [22]. The stars will typically appear two times per year, once during satellite daytime and then again during satellite nighttime up to 7 weeks later. During each appearance, the star may be visible for up to 10 scans per orbit and for approximately 8 consecutive orbits. We refer these as orbital cycles. Since S-NPP and N20 are in the same orbit, the orbital cycles for a given star will occur at the same time, allowing us to compare the response between the two instruments.

In Figure 4, we show example observations for the star HR3905 for consecutive scans and orbits in both instruments. For each scan, the SV DNB data is divided into 4 16x16 pixel sectors, corresponding to the HGA, HGB, MGS, and LGS. The star can be observed in both HGA and HGB in nearly the same location. For certain bright stars, a faint signal can be observed in the MGS, but no signal is measured in the LGS. For SV observations, the aggregation mode is also determined for each scan in a 72-scan cycle, where each of the 32 aggregation modes plus four additional calibration modes are measured for each HAM side. The red dots in Figure 4 show the predicted location of each star in the image, which is determined through aggregation mode spatial mapping [22-23].

In order to accurately use the star observations for calibration stability monitoring and intercomparison, we developed a set of criteria that can be used to identify star observations and filter out data that could be misidentified as a star, such as high-energy particle excitations on the detectors. First, we exclude images with any saturated pixels, which can occur for the brightest stars and also during satellite daytime due to stray light. Next, to register a star detection, we use the brightest pixel in the image of HGA and HGB, with the requirement that the detection location is within one pixel in both images. High-energy particle excitations are unlikely to occur in both HGA and HGB simultaneously at the same location in the images. We also compare the locations of the detections with the predicted positions of the stars from our spatial mapping data. We require that the detections are within 1.2 pixels of the predictions. Finally, we exclude observations where the star detection is on the outside edge of the image, as some signal may be lost.

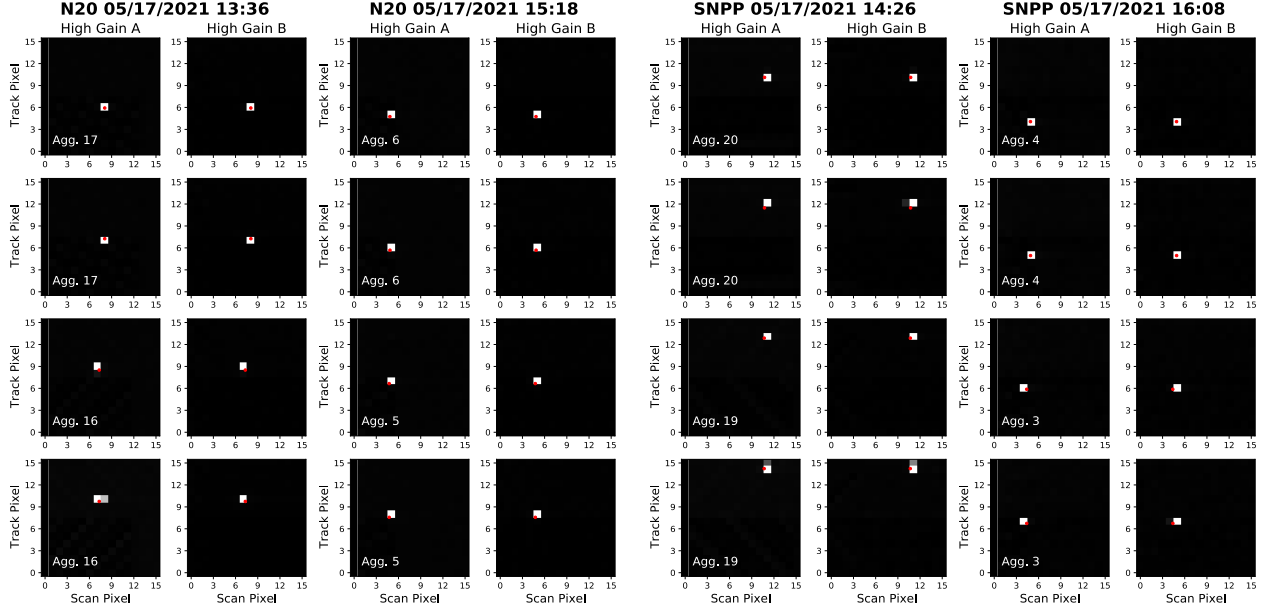


Figure 4. Example star (HR3905) observations from N20 and S-NPP VIIRS DNB (HGA and HGB) on May 17, 2021 over two successive orbits and four scans for each instrument. The predicted location for each observation is shown as a red dot.

To obtain the final signal, we select a 5×5 pixel sub-image centered on the brightest pixel. The outside edge of this area is averaged and used for background subtraction of the sub-image. The inner 3×3 pixel area is then integrated in order to obtain the background-subtracted signal, dn , for both HGA and HGB in each scan. In the rare occurrence of a high-energy particle excitation at the location of the star in either HGA or HGB, we require that the ratio of the HGA to HGB integrated signal be within 30% of unity. We then average the values of HGA and HGB in order to produce our final dn value. To compute the irradiance of each observation, I , we use the following equation:

$$I = F_{HGS} \cdot dn \cdot \Omega \quad (4)$$

Here, F_{HGS} is the F-factor for the high gain stage defined in Equation 3 and Ω is a pixel solid angle correction term that is aggregation mode dependent. In EV data, the aggregation mode changes throughout the scan in order to maintain a nearly constant pixel footprint on ground. Since the SV data uses a single aggregation mode per scan, the overall angular field of view of the SV for different aggregation modes changes in the 72-scan cycle mentioned previously, with near nadir aggregation modes (low number modes) having the largest field of view.

In theory, different detectors, HAM sides, and aggregation modes can have different responses (or gains). As shown in Figures 2 and 3, however, their overall responses are very similar. In order to use all detectors, HAM sides, and aggregation modes together for stability monitoring, a fixed look-up table (LUT) with detector, HAM side, and aggregation mode dependent calibration coefficients is applied to the time-dependent detector responses, thus removing initial calibration differences among detectors, HAM sides, and aggregation modes. For calibration inter-comparison, the F-factors in Equation 4 are from time-dependent calibration LUTs.

4 RESULTS AND DISCUSSION

The scan-level irradiance detailed in the previous section provides a large dataset that can be used to perform calibration assessments for the DNB HGS. In this work, we average all of the scan level data for each star over every orbital cycle over both HAM sides, all detectors, and all aggregation modes. As shown in previous work [16-17], data during spacecraft daytime is impacted by signal from stray light, so the data shown in this work will be for nighttime observations. In Figure 5, we show the normalized response trending for two stars in S-NPP with the pre-launch F -factor applied to all of the data. The points represent the cycle-averaged data during nighttime observations. During the cycle averaging, we apply an iterative 3σ outlier rejection where points that are more than 3 standard deviations from the mean are removed during each iteration. The rejection stops when all data lies within 3σ of the mean. We also require that the remaining data has at least 20 scan level observations for a given orbital cycle in order to keep the data for a given year. The data in Figure 5 shows the average and standard deviation of the remaining points after this outlier rejection for each orbital cycle. We perform this averaging procedure to every star for both S-NPP and N20, and average over both HAM sides, all detectors, and all aggregation modes.

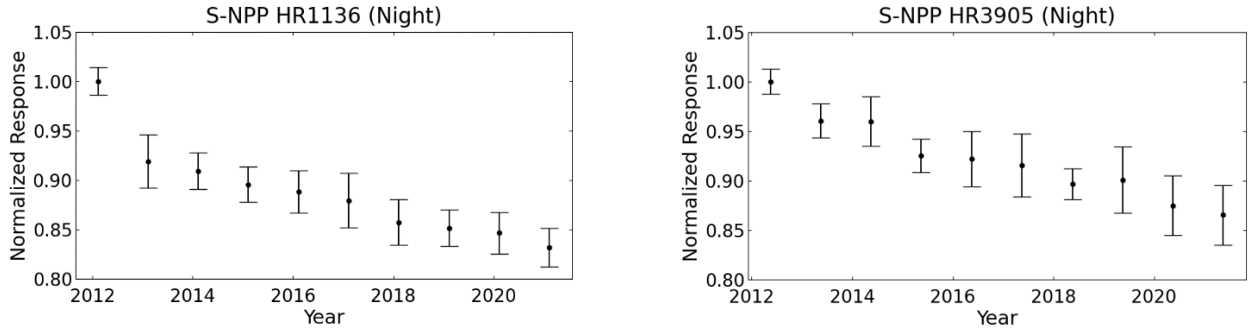


Figure 5. Normalized response (gains or $1/F$) from two stars, HR1136 and HR3905, for S-NPP. Each data point represents the orbital cycle average over both HAM-sides, all detectors, and all aggregation modes. The data is normalized to the value of the first orbital cycle average. The error bars represent ± 1 standard deviation.

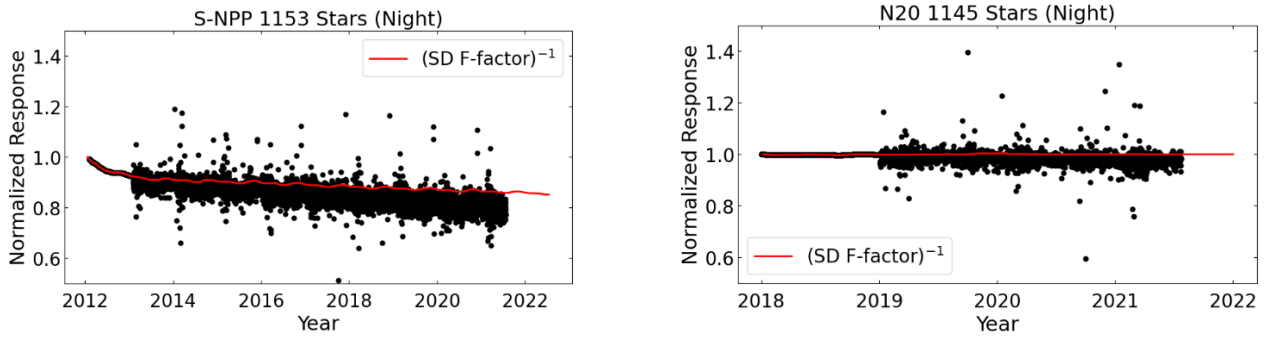


Figure 6. Normalized response (gains or $1/F$) from all available stars for both S-NPP (left) and N20 (right). Each data point represents a cycle average for one star. Each star's time series is normalized to the SD data for its first appearance. The red line shows the inverse of the F -factor derived from SD data for comparison.

As expected, the response level decreases when we apply the fixed pre-launch F -factor in S-NPP, which is associated with a decrease in the sensor gain over the mission. In Figure 6, we compare cycle-average data from more than 1100 stars in both S-NPP and N20 with the detector, HAM-side, and aggregation mode averaged SD F -factor (red). These stars represent all available observations for stars brighter than visual magnitude +6 in the A, B and K stellar temperature classes. Here, the SD F -factor is plotted as the inverse to represent the gain. To make the comparison, each star's cycle-averaged data is normalized to the SD F -factor at time of its first observation. For both instruments, we can see that the overall trending

from SD calibration and star observations are similar and that the star data trends slightly below that of the gain as measured by the SD. The cause of these differences between the SD and star data will need to be investigated.

If we apply the time-dependent HGS F-factors derived from the SD to the star data, we can compute the cycle-averaged irradiance for each star, as seen in Figure 7. Here, we show the trending data for HR1136 for both S-NPP and N20. Since the SD and star derived gains are slightly mismatched (Figure 6), we see a slight downward trend in the irradiance data, especially for S-NPP. In Figure 7, the last 4 data points for S-NPP correspond to the same orbital cycles as the N20 data, allowing us to directly compare the measurements for the same star in both instruments. Since the two plots are on the same scale, we can see from this data that the S-NPP measured irradiance is slightly lower than that of N20 for this star over the same period of the N20 mission.

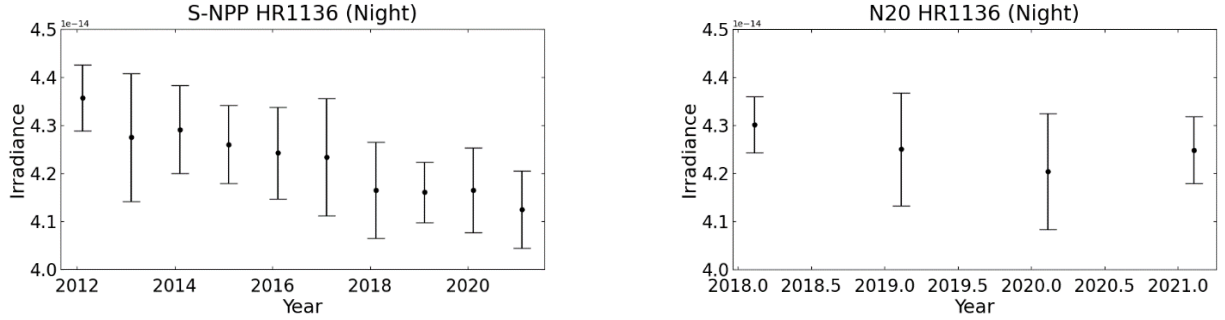


Figure 7. Integrated irradiance cycle averages for HR1136 in both S-NPP (left) and N20 (right). For this data, the time-dependent SD F-factor is applied at the scan level.

To compare the S-NPP and N20 data, we also need to account for the relative spectral response (RSR) differences between the two instruments on-orbit. For S-NPP, contamination of the scan mirror caused changes to the RSR for all bands early in the mission, with a particularly large impact on the DNB owing to its broad spectral range [24]. After the first few years, the S-NPP modulated-RSR stabilized, and there is relatively little change since the launch of N20 in late 2017. To compute the correction factor, we integrate the stellar spectral output for each star weighted by the RSR for each instrument. The stellar spectral data is taken from the INDO-US catalog [25]. Since spectral data is not available for most stars in the BSC (1273 total stars compared to 9110 for the BSC), we match stars with spectral data of the same spectral subclass. For S-NPP, we use the modulated-RSR at the mean time of each orbital cycle averaged data point for each star. The RSR change for N20 on-orbit is negligible, and the pre-launch RSR is used. The irradiance ratio (R) between the two instruments is computed as follows:

$$R_{SNPP/N20} = (I_{SNPP}/I_{N20}) \cdot (\gamma_{N20}/\gamma_{SNPP}) \quad (5)$$

where

$$\gamma_i = \int E^*(\lambda) \cdot RSR_i(\lambda) d\lambda \quad (6)$$

Here, E^* is the stellar spectral irradiance and the subscript, i , represents either instrument, S-NPP or N20. The results for the inter-comparison can be seen in Figure 8. In this figure, we show the results both before (left) and after (right) the spectral correction terms from Equation 6 are applied. The red data shows the ratio of the S-NPP to N20 for each orbital cycle average as determined by Equation 5. The black line shows a linear fit to the red data, and the black points are the average of all of the data available for each calendar year. The error bars show ± 1 standard deviation. For the ratio without spectral correction, the S-NPP response in the HGS is $\sim 6\%$ lower than N20 with a change of -0.1% per year. When the spectral correction is applied, this difference is reduced to $\sim 2\%$, and the slope of the linear fit changes to $+0.17\%$ per year. The spectral correction also reduces the noise observed in the data, which can be attributed to a spread in the ratio among

stars of different spectral temperature classes [22]. Before correction the standard deviation of all of the ratios in Figure 8 is 0.031. This is reduced to 0.023 after the spectral correction is applied.

Compared to previous work, the measured bias between S-NPP and N20 is shifted by $\sim 6\%$ [22]. For the work in [22], the stellar irradiance data for both instruments was computed using the LGS F-factors, which allowed for comparison to other LGS sources such as the Moon. For the star data with the LGS F-factor applied, the S-NPP irradiance was $\sim 4\%$ higher than N20, and for the Moon is $\sim 5\%$ higher. The LGS-to-HGS ratio for both instruments is relatively constant when averaged over all aggregation modes and changes by less than 1%. In both cases, applying LGS and HGS F-factors to the star data, the ratio of the instrument responses between S-NPP and N20 is very stable over the course of the N20 mission. This data will continue to be used to monitor the S-NPP/N20 differences.

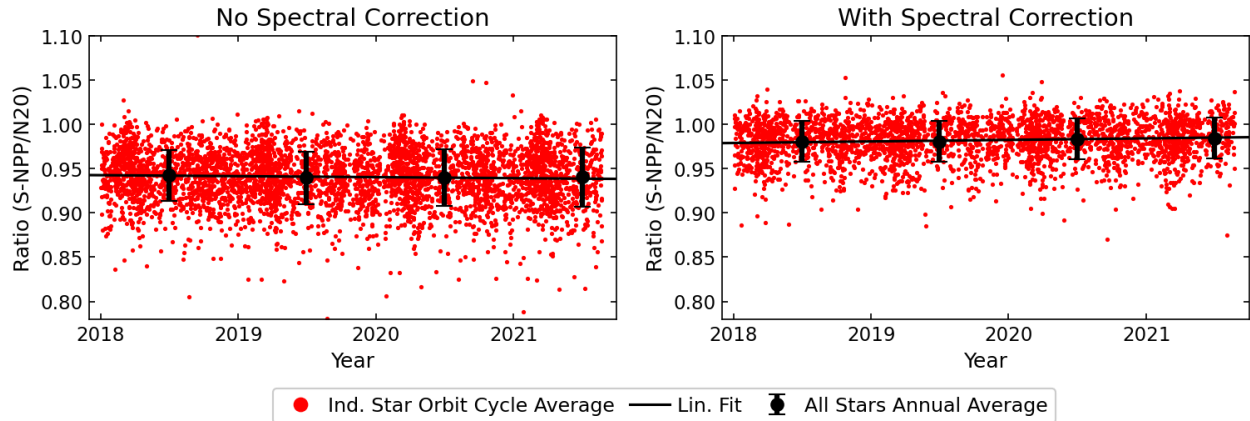


Figure 8. Ratio of the S-NPP and N20 orbital cycle averaged irradiance values (red dots) without (right) and with (left) a spectral correction applied. In the right plot, the modulated RSR is used for S-NPP and the PL RSR is used for N20. The black line shows a linear fit to the red data. The black data points are the annual average of the red data with error bars representing ± 1 standard deviation.

5 SUMMARY

In this work, we used star observations to monitor the DNB HGS gain trending of the VIIRS on board both S-NPP and N20. The star observations are made through the instrument SV port, with the time of appearance determined by the relative orbital geometry of the instrument and the star's coordinates. To minimize the impact due to stray light contamination, we only used the nighttime data in this work. To measure the gain using stars, we developed a set of criteria by which we filter the vast amount of DNB SV data available for each instrument. To improve our signal to noise, we also averaged all of the observations for each star over their respective orbital cycles. Current results show that the star data trends lower than the SD data, especially for S-NPP. The source of this disagreement between the two trends is being investigated. In addition, we have used measurements of the same star in S-NPP and N20 during the same orbital cycles to perform a calibration inter-comparison of the two instruments. From this data, we found that the S-NPP HGS has a response that is $\sim 2\%$ lower than the N20 HGS. This is different from the calibration inter-comparison of DNB LGS, which has S-NPP at a 4-5% higher response level. These differences can be attributed to using different F-factor LUTs in the analysis and an updated spectral correction methodology.

6 ACKNOWLEDGEMENT

The authors would like to acknowledge members of the NASA VIIRS Characterization Support Team (VCST), especially Amit Angal, Hongda Chen, and Chengbo Sun for their contributions and technical support.

7 REFERENCES

1. Cao, C., F. Deluccia, X. Xiong, R. Wolfe, and F. Weng, "Early On-orbit Performance of the Visible Infrared Imaging Radiometer Suite (VIIRS) onboard the Suomi National Polar-orbiting Partnership (S-NPP) Satellite," *IEEE Trans. Geosci. Remote Sens.*, vol. 52, no.2, pp.1142-1156, doi: 10.1109/TGRS.2013.2247768, 2014.
2. Xiong, X., C. Cao, N. Lei, K. Chiang, A. Angal, Y. Li, S. Blonski, W. Wang, T. Choi, "Early Results from NOAA-20 (JPSS-1) VIIRS On-ORBIT Calibration and Characterization", *Proceedings of IGARSS*, 2018, pp. 1112-1115, 2018.
3. Goldberg, M.D., H. Cikanek, L. Zhou, J. Price, "The Joint Polar Satellite System" *Comprehensive Remote Sensing Optical Sensors-VIS/NIR/SWIR*, 2018 ed. Liang, S., Ed., Elsevier: Oxford, UK, 2018, Volume 1, pp. 91–118.
4. Ardanuy, P., C.F. Schueler, S.W. Miller, P.S. Kealy, S.A. Cota, J.K. Haas, C. Welsch, "NPOESS VIIRS Design Process," *Proceedings of SPIE*, 4483, 24-34, 2002.
5. Schueler, C. F., E. Clement, P. Ardanuy, C. Welsh, F. DeLuccia, H. Swenson, "NPOESS VIIRS sensor design overview," *Proceedings of SPIE*, 4483, 11-23, 2002.
6. Lee, T., S. Miller, C. Schueler, S. Miller, "NASA MODIS previews NPOESS VIIRS capabilities," *Weather Forecasting*, 21, 4, 649–655, 2006.
7. Zhou, L., M. Divakarla, X. Liu, A. Layns, M. Goldberg, "An Overview of the Science Performances and Calibration/Validation of Joint Polar Satellite System Operational Products," *Remote Sensing*, 11, 698, 2019.
8. Lee, T., et al. "The NPOESS VIIRS day/night visible sensor," *Bulletin of the American Meteorological Society*, vol. 87, Issue 2, pp.191-199, 2006.
9. Liao, L.B., S. Weiss, S. Mills, B. Hauss, "Suomi NPP VIIRS day-night band on-orbit performance," *Journal of Geophysical Research Atmospheres*, 118(22) 12,705-12,718, 2013.
10. Miller, S.D., et al. "Suomi satellite brings to light a unique frontier of nighttime environmental sensing capabilities," *Proceedings of the National Academy of Sciences* 109(39), 15706-15711, 2012.
11. Román, M.O., Z. Wang, Q. Sun, et al. "NASA's Black Marble nighttime lights product suite," *Remote Sensing of Environment*, 210: 113-143, 2018.
12. Wang, W. and C. Cao, "Monitoring the NOAA operational VIIRS RSB and DNB calibration stability using monthly and semi-monthly deep convective clouds time series," *Remote Sensing*, vol. 8, no. 1, p. 32, 2016
13. Upreti, S., C. Cao, X. Shao, "Radiometric performance characterization of NOAA-20 VIIRS reflective solar bands," *Proc. SPIE* 11501, 1150115, 2020
14. Cao, C., Y. Bai, W. Wang, J. Choi, "Radiometric Inter-Consistency of VIIRS DNB on Suomi NPP and NOAA-20 from Observations of Reflected Lunar Lights over Deep Convective Clouds," *Remote Sensing* 11(8), 934, 2019
15. Mills, S. (2010), VIIRS radiometric calibration algorithm theoretical basis document ATBD, Northrop Grumman, Doc. No.: D43777.
16. Chen, H., X. Xiong, C. Sun, and K. Chiang, "Suomi-NPP VIIRS day-night band on-orbit calibration and performance," *J. Appl. Remote Sens.*, vol 11(3), 36019 2017.
17. Chen, H., X. Xiong, D. Link, C. Sun, K. Chiang, "NOAA-20 Visible Infrared Imaging Radiometer Suite day/night band on-orbit calibration and performance," *J. Appl. Remote Sens.*, 14(3), 034516, 2020.
18. Xiong, X., T. Wilson, A. Angal, and J. Sun, "Using the moon and stars for VIIRS day/night band on-orbit calibration," *Proc. SPIE* 11151, 111511Q, 2019.
19. Wang W. and C. Cao, "NOAA-20 VIIRS DNB Aggregation Mode Change: Prelaunch Efforts and On-Orbit Verification/Validation Results," in *IEEE Journal of Selected Topics in Applied Earth Observations and Remote Sensing*, vol. 12, no. 7, pp. 2015-2023, 2019.
20. Fulbright, J., and X. Xiong, "Suomi-NPP VIIRS day/night band calibration with stars," *Proc. SPIE* 9607, Earth Observing Systems XX, 96071S, 2015.
21. Hoffleit, D. and C. Jaschek, *The Bright Star Catalog*, 5th ed. New Haven, CT, USA: Yale University Observatory, 1991.
22. Wilson, T. and Xiong, X., "Intercomparison of the SNPP and NOAA-20 VIIRS DNB high-gain stage using observations of bright stars," *IEEE Trans. Geosci. Rem. Sens.*, vol. 58, no. 11, pp. 8038-8045, 2020.

23. Wilson, T. and Xiong, X., "Performance assessments of the SNPP and N20 VIIRS DNB using observations of bright stars," Proceedings of SPIE 11530, 1153015, 2020.
24. Lei, N., X. Xiong, and B. Guenther, "Modeling the Detector Radiometric Gains of the Suomi NPP VIIRS Reflective Solar Bands," IEEE Trans. Geosci. Rem. Sens., vol. 53, no. 3, pp 1565-1573, 2015.
25. INDO-US Library. Accessed: Apr. 26, 2019. [Online]. Available: <https://www.noao.edu/cflib>.